VIS and IR bands of Himawari-8/AHI compatible with those of MTSAT-2/Imager

MURATA Hidehiko*, TAKAHASHI Masaya* and KOSAKA Yuki**

Abstract

The Japan Meteorological Agency (JMA) launched Himawari-8 in October 2014 and plans to start its operation in 2015. JMA also plans to launch Himawari-9 in 2016. Himawari-8 and 9 carry a new imager called the Advanced Himawari Imager (AHI). The number of bands will increase to 16 for Himawari-8/9 from 5 for MTSAT-2. In this study, the Himawari-8 bands that are compatible with those of MTSAT-2 were selected for the users who will continue to use only the same bands as those provided by MTSAT-2, and for the HimawariCast service, which disseminates a limited number of bands. For this purpose, simulated satellite images were derived from a radiative transfer model and numerical weather prediction data. These simulated images were then used to compare the characteristics of the Himawari-8 and MTSAT-2 bands. The compatible bands were selected based on the results of this comparison.

1. Introduction

Himawari-8 and 9 are new generation satellites planned by the Japan Meteorological Agency (JMA). Himawari-8 was successfully launched on 7 October 2014, and will start operation in 2015. Himawari-9 is planned to be launched in 2016 (Yokota and Sasaki 2013). Himawari-8 and 9 carry a new imager called the Advanced Himawari Imager (AHI), which is comparable to the GOES-R/Advanced Baseline Imager (ABI) (Schmit et al. 2005). The observation capabilities of Himawari-8/9/AHI are significantly enhanced over those of the MTSAT-2/Imager (Table 1). The number of bands has increased from 5 (VIS 1, IR 4) for the MTSAT-2/Imager to 16 (VIS 3, NIR 3, IR 10) for Himawari-8/9/AHI. Fig.1 shows the Spectral Response Functions (SRFs) of the Himawari-8/AHI and MTSAT-2/Imager. Table 2 shows the central wavelength of these instruments.

The purpose of this study is to select Himawari-8/9/AHI bands which are compatible with those of the MTSAT-2/Imager for users who, even after the start of operation of Himawari-8, will continue to use only the same bands as those provided by MTSAT-2. The compatible bands were selected so as to have similar characteristics to those of MTSAT-2, enabling them to be used in the same manner.

JMA plans to start the HimawariCast service (JMA 2014) via a communication satellite, which disseminates HRIT (High Rate Information Transmission) and LRIT (Low Rate Information Transmission) files of Himawari-8 as a continuation of the HRIT (JMA 2003) and LRIT (JMA 2010) services of the MTSAT series. (Note that the HimawariCast service also disseminates numerical weather prediction products and meteorological observation data such as in-situ observations.) The Himawari-8/AHI data provided by the service will consist of a limited number of bands, 5 bands for HRIT and 4 for LRIT (as of November 2014). The compatible bands selected in this study will be the ones used by the service.

Only comparisons of central wavelength or shape of SRFs between the two instruments are usable for the selection of compatible bands. However, monochromatic radiation properties such as scattering by ice/water particles and atmospheric molecular absorption differ according to wavelength, with atmospheric molecular absorption being especially sensitive. It is therefore necessary to take the total effect of the instruments' SRFs into account. Furthermore, the similarity/difference of bands depends on various atmospheric conditions. In this study, in order to take the above into consideration,

* System Engineering Division, Data Processing Department, Meteorological Satellite Center

** Numerical Prediction Division, Forecast Department, Japan Meteorological Agency

(Received August 6, 2014, Accepted February 13, 2015)

synthetic satellite images were simulated from a radiative transfer model and numerical weather prediction data. In recent years, simulated satellite images have also been used to demonstrate the capabilities of future instruments, and to develop satellite products with a reliable degree of accuracy (e.g. Otkin et al. 2007; Bormann et al. 2014). Details regarding simulated satellite images are described in Section 2.

The compatible bands were selected by comparing simulated image snapshots. Selection focused mainly on similarity, i.e., on there being a high degree of correlation between the simulated images from Himawari-8 and those from MTSAT-2. Details of the comparison for each band are given in Section 3. The similarities/differences of the instruments are also covered in this section, providing useful information for users using MTSAT-2 and Himawari-8 in the future.

The final selection is shown in the Table 2. Note that although the selected compatible bands have similar characteristics to the MTSAT-2 bands, they are not exactly the same.

Table 1: Specification of Himawari-8/9/ AHI and MTSAT-2/Imager

	Himawari-8/9/AHI	MTSAT-2/Imager
Number of bands	Total of 16 VIS 3, NIR 3, IR 10	Total of 5 VIS 1, IR 4
Spatial resolution at sub-satellite point	0.5 km, 1 km, 2 km	1 km, 4 km
Observation interval	Every 10 min. for full disk observation	Every 30 min. for full disk or north hemisphere observation

Table 2: VIS and IR bands of Himawari-8/AHI and MTSAT-2/Imager. Each MTSAT-2/Imager band is shown on the same line as the corresponding compatible Himawari-8/AHI band selected in this study.

Himawari-8/AHI		MTSAT-2/Imager	
Band	Wavelength (μm)	Band	Wavelength (μm)
#1	0.47		
#2	0.51		
#3	0.64	VIS	0.68
#4	0.86		
#5	1.6		
#6	2.3		
#7	3.9	IR4	3.7
#8	6.2	IR3	6.8
#9	6.9		
#10	7.3		
#11	8.6		
#12	9.6		
#13	10.4	IR1	10.8
#14	11.2		
#15	12.4	IR2	12.0
#16	13.3		

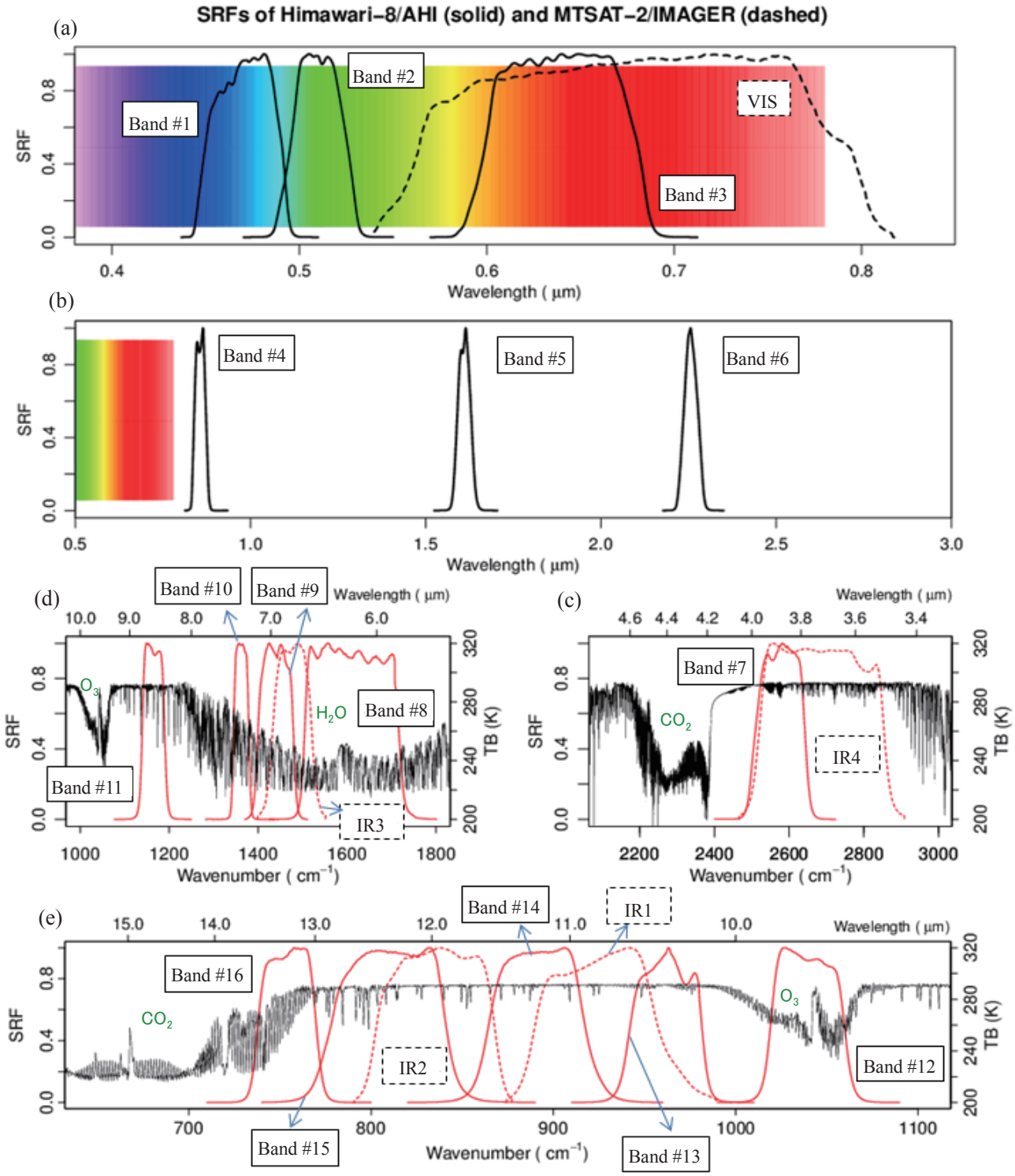

Fig.1: The two upper panels show the SRFs for (a) VIS and (b) NIR for Himawari-8/AHI (solid black line) and MTSAT-2/Imager (dashed black line). The background in these panels shows the color of visible light at the corresponding wavelength. The three panels (c), (d) and (e) show the SRFs for IR for Himawari-8/AHI (solid red line) and MTSAT-2/Imager (dashed red line). The thin black line in these panels indicates the brightness temperature of the outgoing radiation at the top of the atmosphere calculated from the HITRAN2000 database using the radiative transfer model of LBLRTM for the US standard atmosphere. The major atmospheric molecules contributing to absorption are

shown in green letters. The “Band #1” to “Band #16” labels indicate the Himawari-8/AHI bands, and "VIS” and “IR1” to “IR4" indicate the MTSAT-2/Imager bands.

2. Simulated Satellite Images

In this study, simulated satellite images were used to compare Himawari-8/AHI with the MTSAT-2/Imager. These simulated images were derived from RSTAR (Nakajima and Tanaka, 1986; Nakajima and Tanaka, 1988; Stamnes et al., 1988), which is a radiative transfer model developed by the Atmosphere and Ocean Research Institute at the University of Tokyo.

Table 3 shows the design of the RSTAR-based radiative transfer calculation. The atmospheric profiles input into RSTAR are the analysis and forecasts output from the JMA Global Spectral Model (GSM, JMA 2013). For surface conditions, a MODIS surface reflectance product provided by NASA was used (Vermote et al. 2011). The climatological parameters used in the GSM were adopted for ozone (Maki et al. 2008) and aerosol (JMA 2013).

Fig.2 shows examples of the approximated SRF used in RSTAR. The left panel (a) shows SRFs for MTSAT-2 VIS and Himawari-8 band #3, and the right panel (b) shows those for MTSAT-2 IR1 and Himawari-8 band #13. The approximated SRFs, represented by 10 points, are shown as a stepped line, whose height is the same as the original SRF at the center of each sub-wavelength grid. The total radiance of the band is a weighted average of all the sub-wavelength grid radiances.

The optical depth of ice/water cloud used in RSTAR for calculation of cloud affected radiance is retrieved from the cloud water content and cloud cover in the GSM (based on Owada 2006). In RSTAR, ice cloud particles are assumed to be hexagonal plates (Yang et al. 2000). In order to save calculation time, cloud overlap is not taken account.

The radiances calculated by RSTAR are converted into reflectivity (for visible bands) or brightness temperature (for infrared bands). Reflectivity is radiance normalized by solar irradiance for each band calculated by RSTAR (i.e. reflectivity = $\pi I/S_0$, where I is radiance and S_0 is the solar irradiance for the band). Note that neither the correction for solar zenith angle nor sun-earth distance fluctuation is applied to the reflectivity. For the infrared bands, radiances are converted into brightness temperatures by the sensor-Planck function (Tahara 2008) which takes account in the SRF of the correction to the monochromatic Planck function. In this case, quadratic coefficients are applied.

Fig.3 shows simulated and observed full-disk images for the MTSAT-2/Imager; (a) and (b) are for IR1, and (c) and (d) are for VIS. Histograms (e) and (f) show the corresponding brightness temperature/reflectivity distributions. The observation values are averaged over boxes subtended by 0.2 by 0.2 degrees to fit the grid spacing of the GSM (approximately 20 km).

The first impression of simulated images (a) and (c) is that they seem to be realistic. Visual comparisons with the real images focusing on synoptic scaled cloud system distributions ((a) and (b) for IR1; (c) and (d) for VIS) show that both bands are generally in good agreement. Histograms (e) and (f) also show a similar dynamic range and shape.

However, some discrepancies can be identified from a detailed comparison of the maps and histograms. It can be inferred that the difference in cloud positions in the maps is associated with the GSM forecasting error.

With regard to cloud cover, there are excessive low level clouds in the simulated images, these being especially recognizable in visual comparison of VIS images (c) and (d). The histogram of VIS reflectivity (f) shows that the frequencies in the simulated image are higher at high reflectivity (over 0.3) corresponding to low level clouds, and in contrast are lower at low reflectivity corresponding to absence of low level clouds. In the histogram of IR1 brightness temperature (e), the frequencies for the simulated image are higher around 270-290K, corresponding to the quantity of low level

clouds.

Furthermore, it is found that the frequency of cold brightness temperatures of 200-250K is lower in IR1 histogram (e), corresponding to the less thick and high top clouds in simulated IR1 image (a). It is likely that these discrepancies are related to a bias in humidity in GSM (Miyamoto et al. 2009). Owada (2006) also discussed the overestimation of lower clouds and underestimation of thick high clouds in simulated satellite images derived from GSM.

Nevertheless, these discrepancies between simulated and real observed images are relatively unimportant in this study, since its purpose is to focus only on the general similarities and differences of the radiation characteristics of the bands within the simulated images. For this reason, no further details of the differences between simulated and real observed images are discussed here.

In this study, it is assumed that, for the current purpose, the simulated satellite images produced by RSTAR are of sufficient practical accuracy.

Table 3. Radiative transfer calculation design

Targeted calculation time	06 UTC on 28 September 2012 (Forecast time=0h)
Radiative transfer model	Rstar6b
Longitude of sub-satellite point	140°E
SRF (Spectral Response Function)	Approximated by 10 points
Number of vertical layers	14 layers (0-1 km, 1-2 km, 2-3 km, 3-4 km, 4-5 km, 5-6 km, 6-7 km, 7-8 km, 8-9 km, 9-10 km, 10-20 km, 20-50 km, 50-80 km, 80-120 km)
Atmospheric profiles	GSM (TL959L60, reduced Gaussian 20 km grid spacing) (JMA 2013)
Surface wind speed	GSM
Surface reflectance	MODIS Surface-Reflectance Product (MOD 09) (Vermote et al. 2011)
Aerosol optical depth	Total-column climatology value used in GSM
Cloud optical depth (ice/water)	Retrieved from GSM cloud water content and cloud cover (Ice crystal habits: hexagonal plates, Yang et al. 2000)
Ozone	3D Climatological ozone used in GSM (Maki et al. 2008)

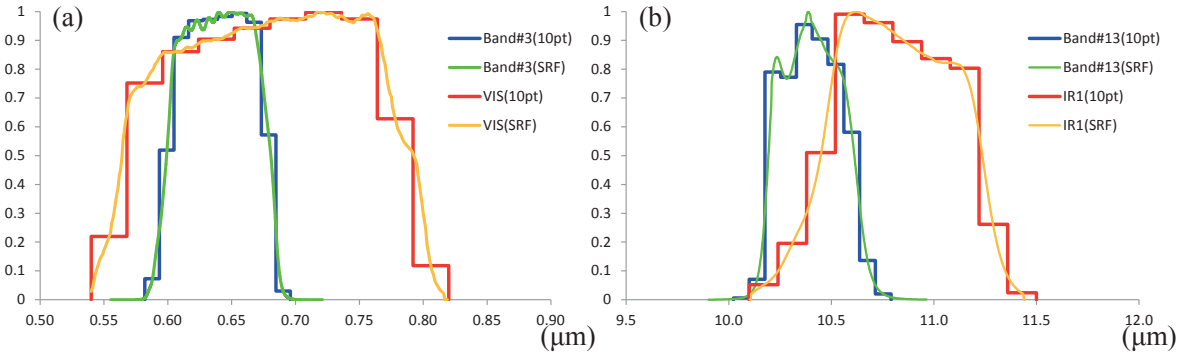

Fig.2: Examples of SRF for (a) MTSAT-2 VIS and Himawari-8 band #3 and (b) MTSAT-2 IR1 and Himawari-8 band #13. The orange (MTSAT-2) and green (Himawari-8) lines are the original SRFs, and the red (MTSAT-2) and blue (Himawari-8) lines are approximated SRFs represented by 10 points.

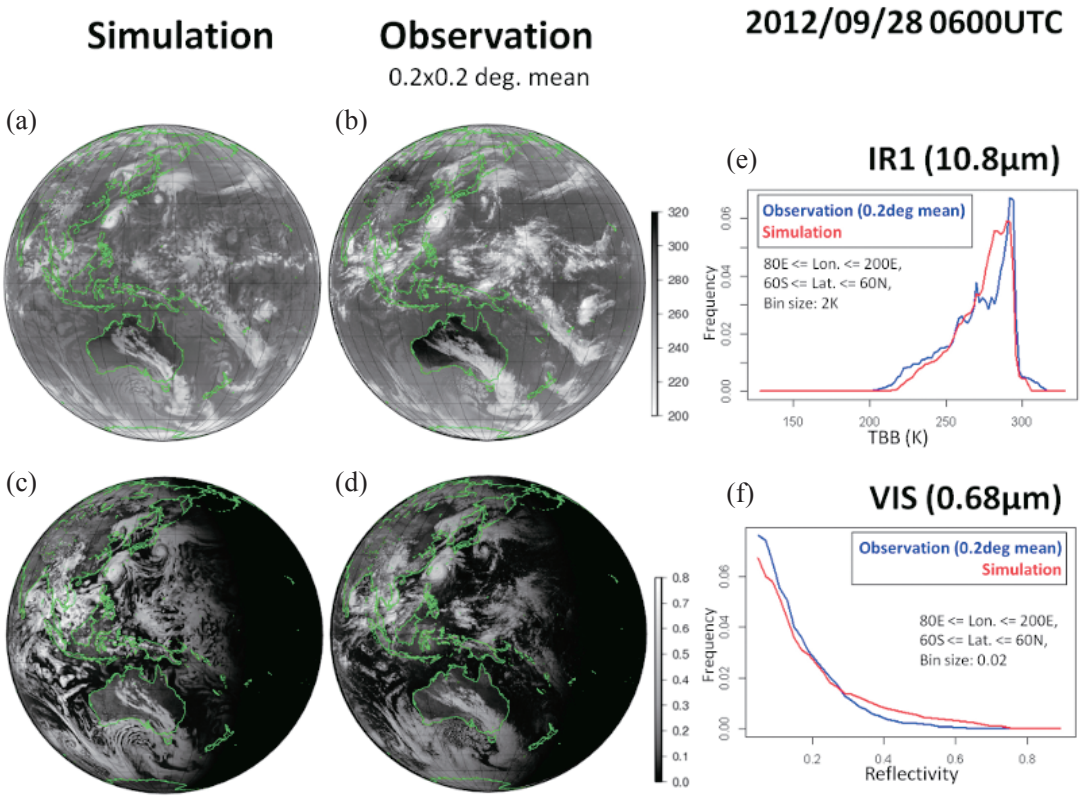

Fig.3: Comparisons between simulated images (left) and real observed images (middle) for MTSAT-2 at 06 UTC on 28 September 2012. The observed images are averaged over boxes of 0.2 by 0.2 degrees. The upper images show the brightness temperature for IR1, and the lower images show the reflectivity for VIS. The two panels on the right show histograms of brightness temperature and reflectivity (blue: averaged observed value, red: simulated value).

3. Study of compatible bands

In this section, the compatible Himawari-8/AHI bands for each of the MTSAT-2/Imager bands are investigated by comparing the simulated images for each instrument. Reflectivity is compared for visible bands, and brightness temperature for infrared bands. Although MTSAT-2 is actually located at 145 degrees east, in the simulation, its sub-satellite point was placed at 140 degrees east to make it the same as Himawari-8.

First, some candidate Himawari-8 bands were picked out by referring to the central wave lengths (Table 2) and SRFs (Fig.1). Simulated images of the candidate Himawari-8 bands and their corresponding MTSAT-2 band were then compared using 2-dimensional histograms and full-disk difference maps. In the 2-dimensional histograms, the points with a zenith angle of less than 75 degrees were plotted in order to focus on the data used in actual situations. The inner circle of the full-disk maps in Figs.4, 5, 7 to 9 and 11 shows the 75 degree satellite zenith angle line.

The set of simulated images used in this study is only a snapshot (06 UTC on 28 September 2012). However, the simulated full-disk image contains a variety of weather and solar illumination conditions. Hence, the full-disk simulated image was able to provide comprehensive information sufficient for this study.

The basic focus of compatible band selection was to provide a high correlation between the two instruments over the full-disk image. In some cases, aspects regarding use of the band were also taken into account.

3.1. VIS

Himawari-8/9/AHI has three visible bands corresponding to the colors blue (band #1, 0.47 μm), green (band #2, 0.51 μm) and red (band #3, 0.64 μm). Fig.1 (a) shows that, although the SRF of Himawari-8 band #3 is narrower, there is a very good overlap with that of MTSAT-2 VIS (0.68 μm).

Fig.4 shows comparisons between simulated reflectivity for the Himawari-8 visible bands and that for MTSAT-2 VIS. As can be seen from 2-dimensional histogram (c), the reflectivity of Himawari-8 band #3, with its higher correlation and lower bias, shows the best correspondence to that of MTSAT-2 VIS.

The differences in reflectivity are shown in the lower panels. Band #3 shows the best correspondence and smallest differences (map (f)), consistent with the 2-dimensional histograms above.

The overall differences for bands #1 and #2 are more positive where the solar illumination is dominant (western part of the disk). This is caused mainly by the difference in Rayleigh scattering. Conversely, the differences are negative over cloud free land, as seen in the western part of Australia and inland China. These areas are covered with dry soil, and for this type of surface, reflectivity generally increases with wavelength within the visible wavelength range (Clark et al., 2007). This corresponds to the low reflectivity region of the 2-dimensional histograms (upper panels), in which variation is relatively large.

From these results, Himawari-8 band #3 was selected as the compatible band for MTSAT-2 VIS.

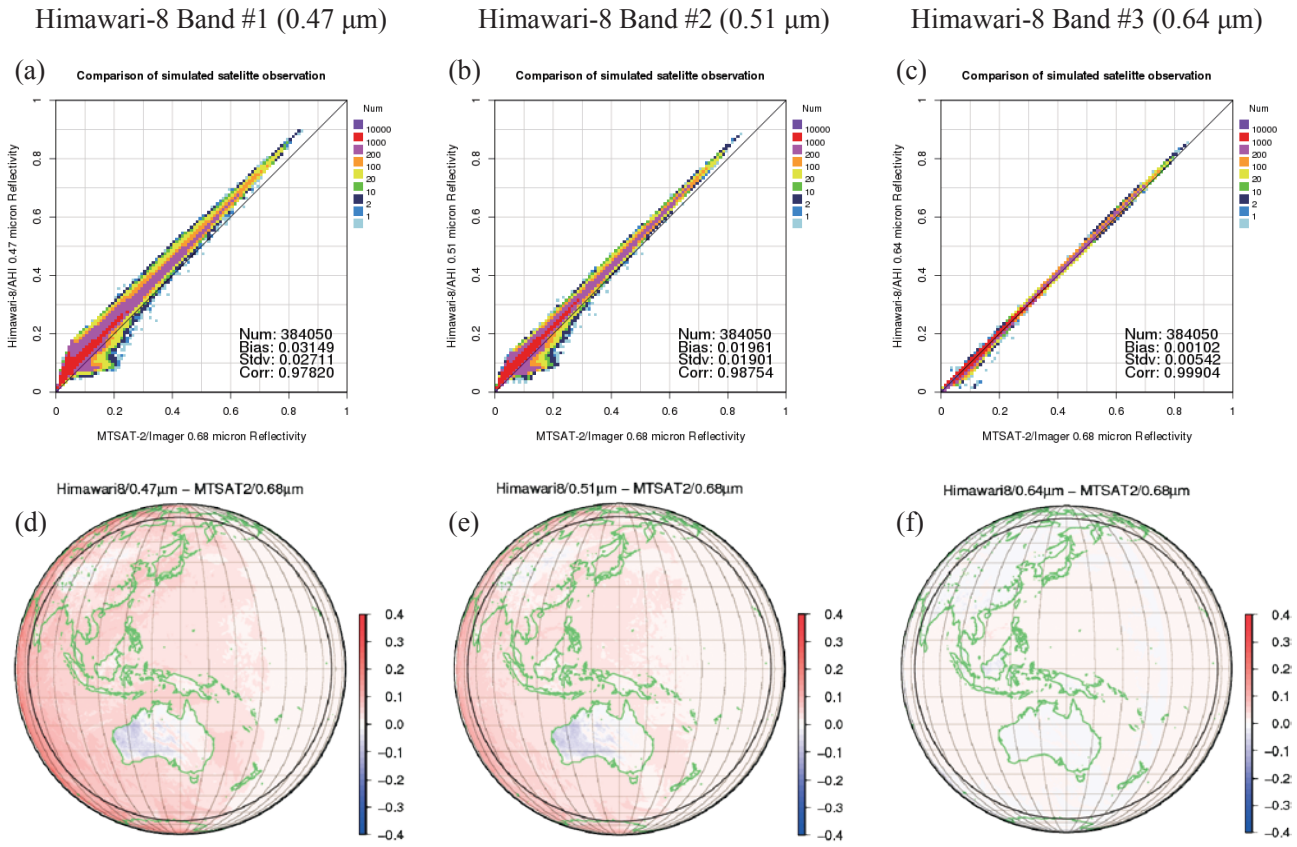

Fig.4: Comparisons of simulated reflectivity for MTSAT-2/Imager VIS (0.68 μm) against that for Himawari-8/AHI bands #1 (0.47 μm) (left), #2 (0.51 μm) (middle) and #3 (0.64 μm) (right) at 06 UTC on 28 September 2012. The upper panels show 2-dimensional histograms with MTSAT-2/Imager VIS reflectivity on the horizontal axis and Himawari-8/AHI reflectivity for bands #1, #2 and #3 on the vertical axis. The color represents the number of points in the bins. The lower images show the differences in reflectivity between MTSAT-2/Imager VIS and Himawari-8/AHI bands #1, #2 and #3. The inner circle of the maps shows satellite zenith angle=75 degrees, and the points within the circle are those plotted in the 2-dimensional histograms.

3.2. IR4

As can be seen in Fig.1 (c), the SRF of Himawari-8 band #7 (3.9 μm) has the closest distribution to that of MTSAT-2 IR4 (3.7 μm), and there are no other candidates for this band. The Himawari-8 SRF is narrower, with the MTSAT-2 SRF showing a wide spread towards shorter wavelengths.

Fig.5 shows a comparison between simulated brightness temperatures for Himawari-8 band #7 and those for MTSAT-2 IR4.

As indicated in the 2-dimensional histogram of brightness temperature (a), there is a high correlation between Himawari-8 band #7 and MTSAT-2 IR4. In the daytime area, brightness temperatures include reflected solar radiation; these observed temperatures are therefore warmer than those from the Earth alone. In order to take the effect of solar radiation into account, the 2-dimensional histograms are divided according to solar condition into (c) the daytime area (solar zenith angle < 80 deg.) and (d) the nighttime area (solar zenith angle > 93 deg.). In the daytime area, the overall difference is negative over cloudy areas, as shown in (b) (i.e. less

reflective for Himawari-8). This is probably because the SRF of Himawari-8 band #7 spreads toward shorter wavelengths where the effect of solar radiance is more significant. In the nighttime area, the radiation is only from the Earth. The two instruments are in good agreement, with very small differences and a high correlation (see (d)).

As a result, Himawari-8 band #7 was adopted as the compatible band for MTSAT-2 IR4.

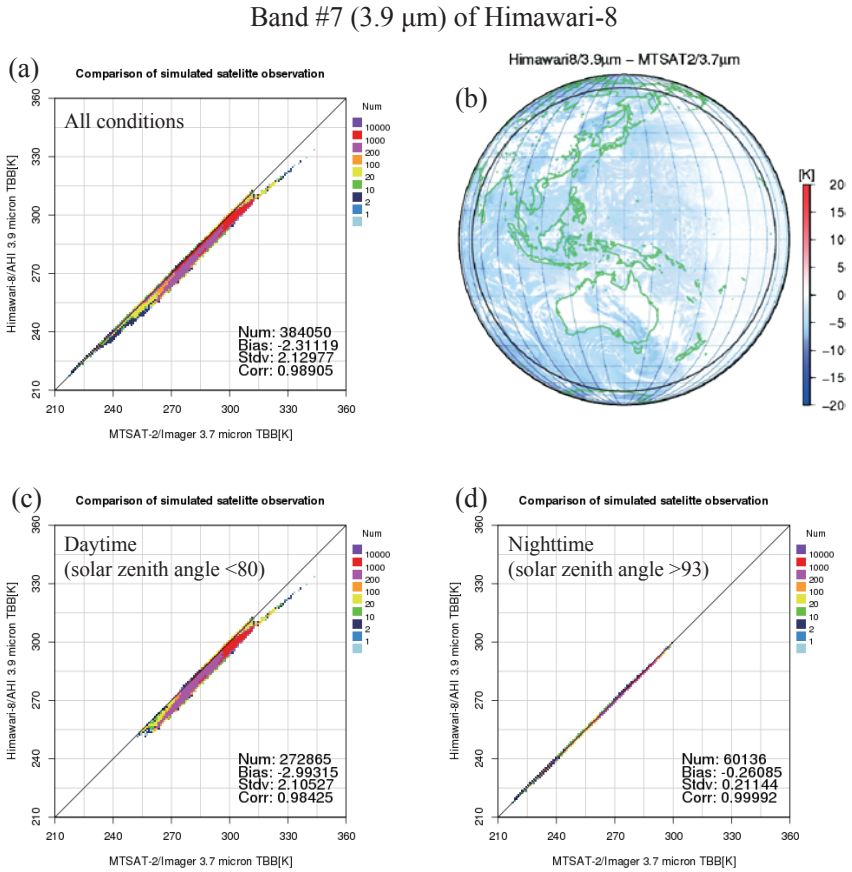

Fig.5: Comparisons of simulated brightness temperature for MTSAT-2/Imager IR4 (3.7 μm) against that for Himawari-8/AHI band #7 (3.9 μm). The 2-dimensional histograms show MTSAT-2 brightness temperature on the horizontal axis and Himawari-8 brightness temperature on the vertical axis for (a) all conditions, (c) daytime (solar zenith angle < 80 deg.) and (d) nighttime (solar zenith angle > 93 deg.). The differences in brightness temperature between MTSAT-2/Imager IR4 and Himawari-8/AHI band #7 are shown in (b).

3.3. IR3 (WV)

There are three possible candidates for the Himawari-8 band compatible with MTSAT-2 IR3 (6.8 μm): band #8 (6.2 μm), #9 (6.9 μm) and #10 (7.3 μm) located in the water vapor absorption band (Fig.1 (d)). Water vapor band images are often used to determine the synoptic upper troposphere structure, such as jet, trough and ridge of mid-latitudes, for daily weather forecasting.

For a visual comparison of WV bands, Fig.6 shows simulated and real observed images of Eastern Asia. The simulated and observed MTSAT-2 IR3 images are shown in Figs. 6 (a) and (b). Comparison reveals that, although there are some discrepancies in detailed cloud distribution, the structure of the water vapor shade pattern of the simulated image is generally realistic. From a comparison of the simulated Himawari-8 images (c),

(d) and (e) with (a) for MTSAT-2 IR3, it can be seen that the water vapor shade pattern is well represented by bands #8 and #9.

From the 2-dimensional histograms (upper panels in Fig.7), it can be seen that the brightness temperature for Himawari-8 band #8 shows the highest correlation with that of MTSAT-2 IR3 (the correlation of 0.99566 is the highest of the 3 bands and is statistically significant, with $p<0.01$).

The lower panels in Fig.7 show the differences between the Himawari-8 bands and MTSAT-2 IR3. Generally, these are negative for band #8 and positive for bands #9 and #10. As a result of these negative (positive) differences, the brightness temperature of Himawari-8 is colder (warmer) and the layer of peak sensitivity is higher (lower) than for MTSAT-2.

From these comparisons, it was decided that Himawari-8 band #8 be selected as the compatible band for MTSAT-2 IR3. However, it should be noted that the brightness temperatures are slightly colder than for MTSAT-2 IR3.

Even though band #9 has the closest central wavelength (Table 2) and the SRF with the largest overlap (Fig.1 (d)), band #8 is the most similar to MTSAT-2 IR3 in terms of its radiative characteristics. This result was obtained using radiative transfer calculations that take account of the total absorption of water vapor within the SRF. It was concluded that the method used in this study constitutes a valuable technique.

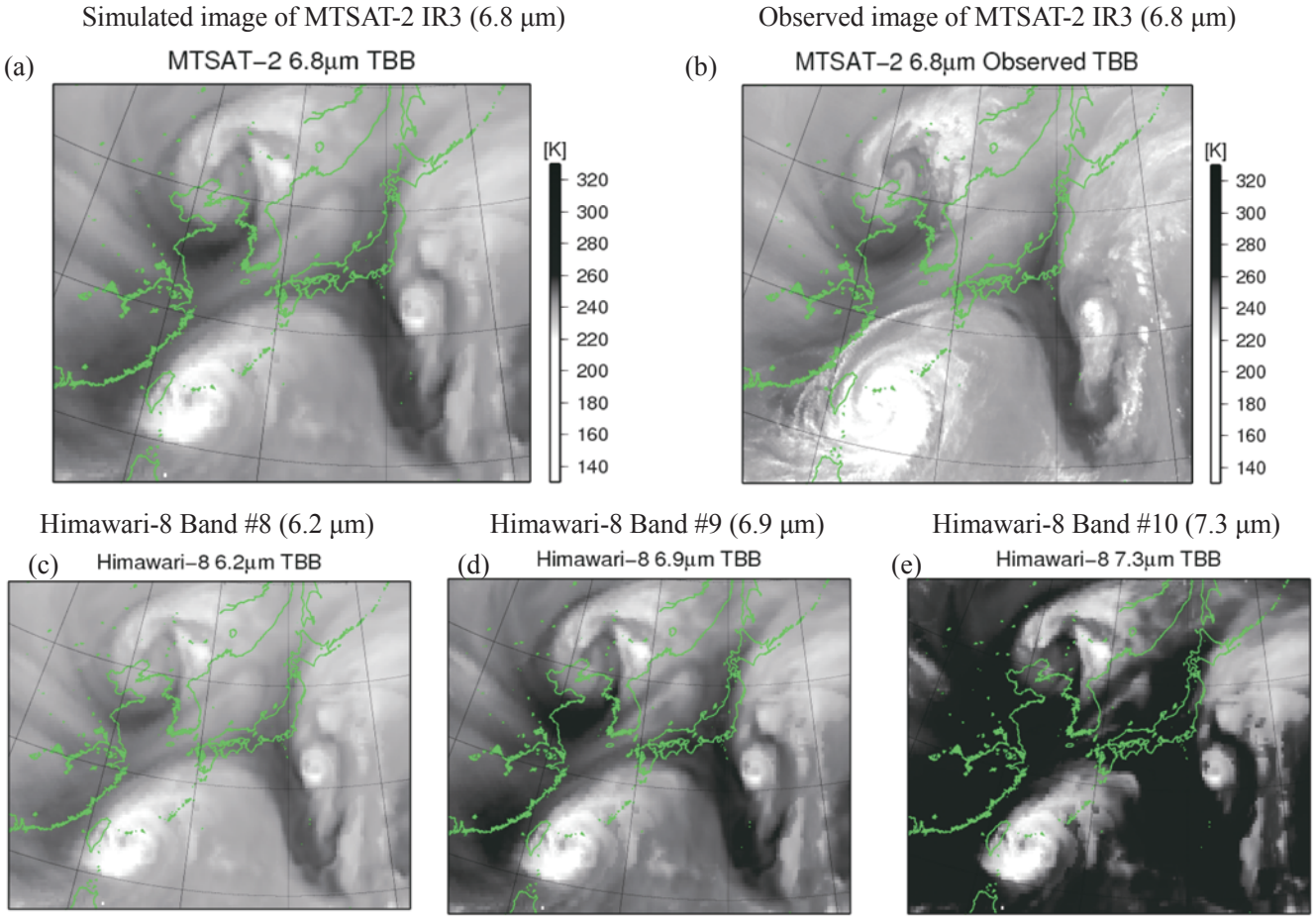

Fig.6: (a) Simulated image of MTSAT-2/Imager IR3, and (b) observed image of MTSAT-2/Imager IR3; (c), (d) and (e) simulated images of Himawari-8/AHI bands #8 (6.2 μm), #9 (6.9 μm) and #10 (7.3 μm) (bottom). The color scale of all

images is the same.

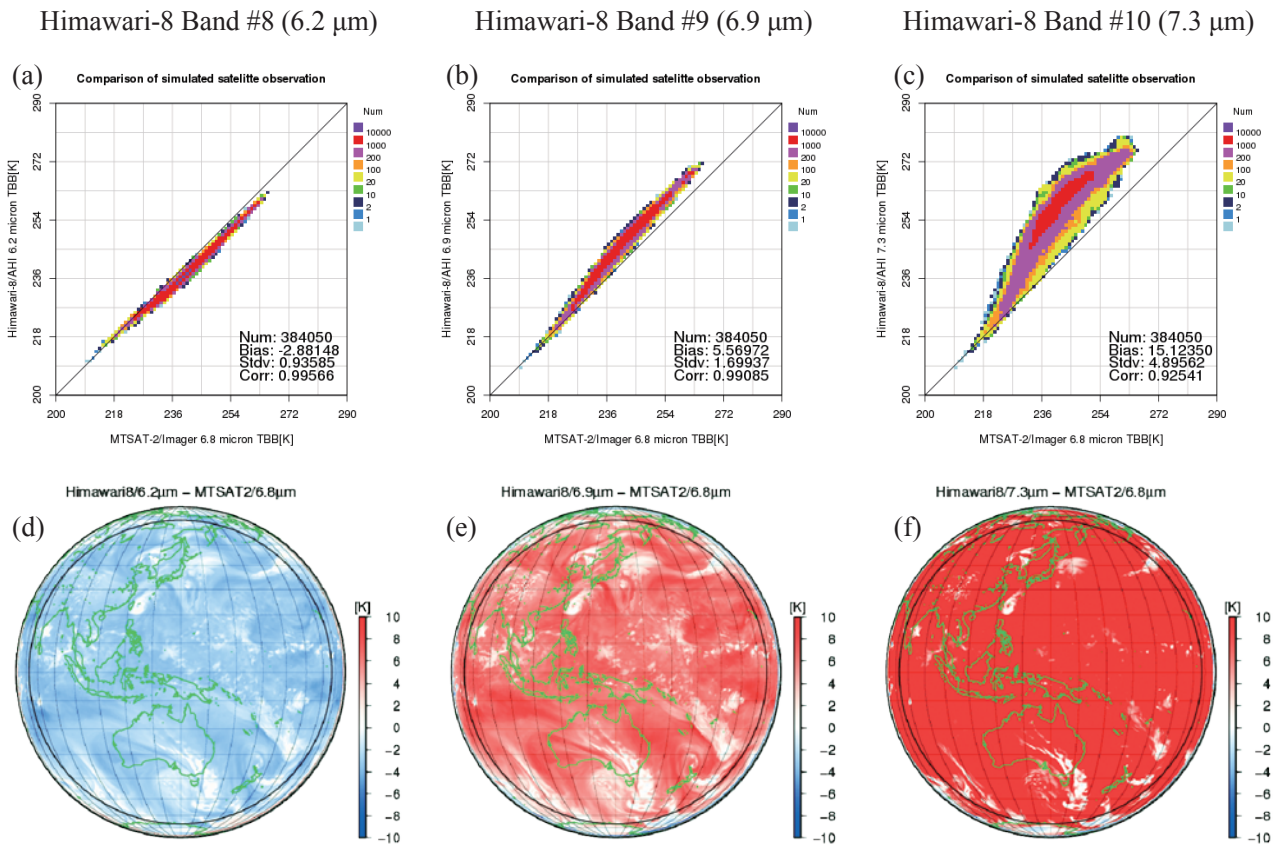

Fig.7: Same as Fig.4, except for comparisons between the simulated brightness temperature for MTSAT-2/Imager IR3 (6.8 μm) and that for Himawari-8/AHI bands #8 (6.2 μm) (left), #9 (6.9 μm) (middle) and #10 (7.3 μm) (right).

3.4. IR1 and IR2

MTSAT-2 IR1 (10.8 μm) and IR2 (12.0 μm) are located in the "atmospheric window" around 10 to 12 μm, which has less absorption by atmospheric molecules (Fig.1 (e)). In investigating selection of the compatible band for these window bands, utilization of the combination of IR1 and IR2, which constitute split window (hereafter SW) bands, was also considered. The brightness temperature difference (BTD) between SW bands is used for detection of thin cirrus, lower clouds and volcanic ash, and for SST retrieval to eliminate water vapor effects, etc.

From a comparison of the SRFs in Fig.1 (e), the candidate bands for MTSAT-2 IR1 are seen to be Himawari-8 bands #13 (10.4 μm) and #14 (11.2 μm). For reference, band #15 (12.4 μm) was also compared. The candidate bands for IR2 are bands #14 and #15, and band #16 (13.3 μm) was also compared for reference.

Comparisons of bands #13, #14 and #15 with IR1 are shown in Fig.8. The 2-dimensional histograms (upper panels) show that both candidate bands #13 and #14 have a very high correlation (0.99930 and 0.99929 for #13 and #14, respectively).

The map of difference between #13 and IR1 (d) shows that these are generally slightly negative except for areas of cloud, the brightness temperature being slightly lower for band #13 than for IR1. This result is consistent with

the study of Lindsey et al. (2012), which showed the characteristics of the GOES-R/ABI 10.35 μm band, whose SRF is close to that of band #13. This band is less sensitive to water vapor absorption (i.e. is referred to as a "cleaner" band) but instead is slightly affected by absorption of O_3 and CO_2. Brightness temperature is therefore slightly colder than for 11 μm under relatively dry conditions. (In this case, MTSAT-2 IR1 (10.8 μm) can be considered in place of the 11 μm band.) The negative area is spatially less noisy than the difference between band #14 and IR1 (map (e)). This is because the dry gasses (O_3 and CO_2), which mainly affect the difference, are more horizontally homogeneous than water vapor, which is more dominant for band #14.

The pattern of difference between band #14 and IR1 (e) is similar to the inversed SW pattern shown in Fig.10, which will be discussed later. This is because the wavelength relationship of IR1 (10.8 μm) and band #14 (11.2 μm) is similar to the role of the SW bands.

Comparison between band #15 and IR1 (Fig.8 right column) shows that correlation is somewhat lower (0.99442) than in the case of the other two bands, and the difference is generally negative and larger, so that it is not suitable as the compatible band.

Comparisons of band #14, #15 and #16 with IR2 are shown in Fig.9. The 2-dimensional histograms (upper panels) show that both candidate bands #14 and #15 have a very high correlation (0.99892 and 0.99952 for #14 and #15, respectively).

The map of difference between band #14 and IR2 (d) is generally positive, and between band #15 and IR2 (e) is generally negative. This is because the effect of water vapor absorption increases with wavelength in the "atmospheric window". Band #14 is less affected and, conversely, band #15 is more affected by water vapor than IR2. Hence, the general difference in brightness temperature is caused by the difference in the effect of water vapor.

The SRF of band #16 spreads over the CO_2 absorption band at around 15 μm (Fig.1 (e)), and is no longer in the "atmospheric window". Hence, the correlation between #16 and IR2 is somewhat lower (0.98179) than in the case of the other two bands, and the difference in brightness temperature is larger. Band #16 is therefore not suitable as the compatible band.

The simulated and observed BTD images for MTSAT-2 SW are compared in Fig.10, in order to confirm whether the simulated BTD images for SW are also realistic. In general, most areas of both of the images are commonly positive. The features of the BTD are well represented in the simulated image, such as thin cirrus along with thick cloud (e.g. the large cloud area spreading northwest to southeast over Australia). It was therefore concluded that these simulated BTD images for SW were also suitable for use in this study. There are negative BTDs around the limb of the disk only in the simulated image. This may indicate that the accuracy of the radiative transfer calculation is lower in the limb area, in which satellite zenith angle is significantly large.

The BTDs for the combinations of Himawari-8 bands forming possible candidates for selection, i.e. bands #13-#14, #14-#15, and #13-#15, are shown in Fig.11. The positive/negative pattern of #13-#15 (Fig.11 (c)) is similar to the MTSAT-2 SW image (Fig.10 (a)).

Fig.12 shows 2-dimensional histograms of the simulated BTDs for MTSAT-2 and Himawari-8 SW. As shown in Fig.11, the pattern of the #13-#15 SW BTD exhibits the greatest similarity to that of MTSAT-2, showing strong linearity and the highest correlation with MTSAT-2 (0.99114), and crossing the origin (Fig.12 (c)). The steeper slope of the 2-dimensional histogram gives a higher contrast image for band #13-#15 BTD (Fig.11 (c)) than for MTSAT-2 SW (Fig.10 (a)). The higher contrast is somewhat beneficial with regard to detection of the items mentioned earlier.

In summary, for IR1, bands #13 and #14 have a high correlation (which may be slightly better for #13), and for IR2, bands #14 and #15 have a high correlation (which may be better for #15). In addition, considering the use of SW, the combination of #13-#15 has a high correlation to IR1-IR2, and its enhanced SW BTD contrast is beneficial

to use. From the above, Himawari-8 band #13 was selected as the compatible band for MTSAT-2 IR1, and band #15 as compatible with IR2.

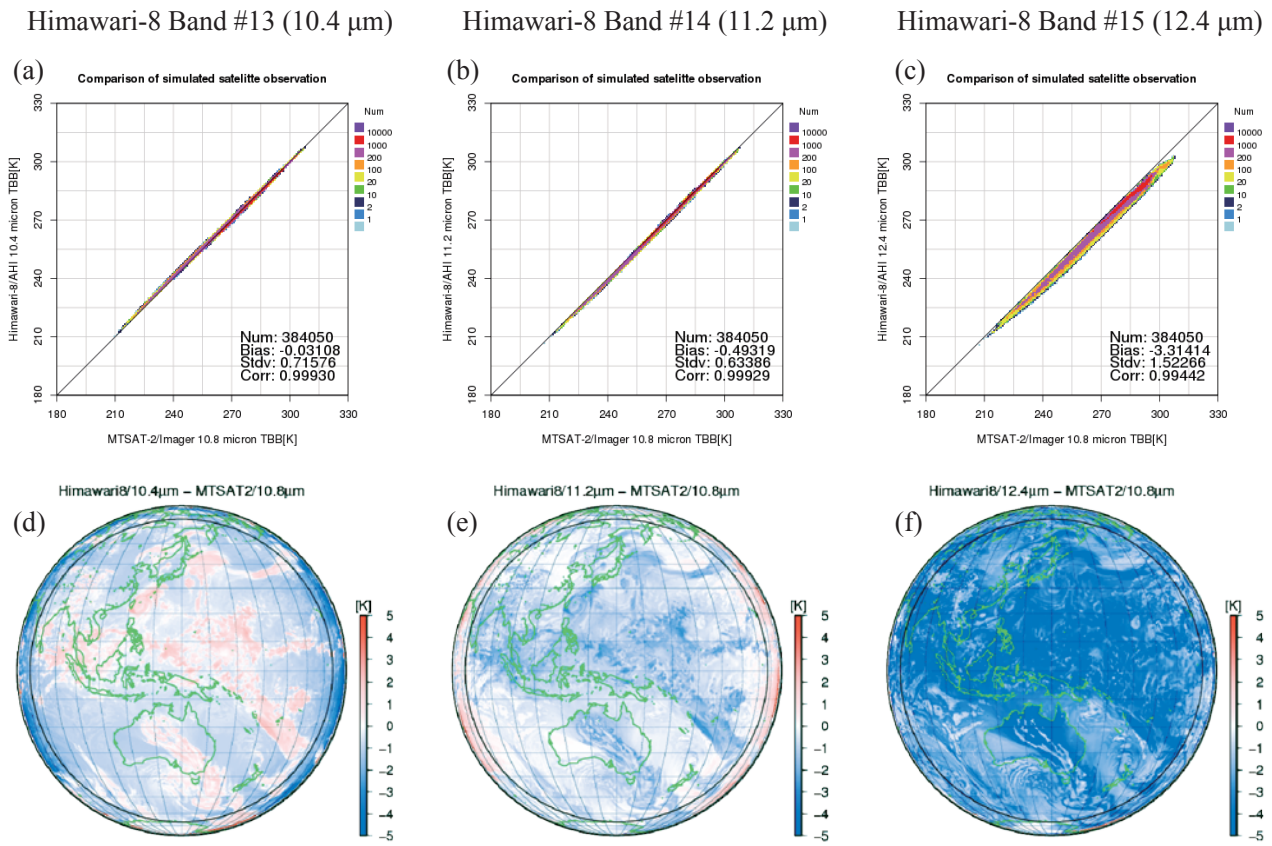

Fig.8: Same as Fig.4, except for comparisons of the simulated brightness temperatures for MTSAT-2/Imager IR1 (10.8 μm) against those for Himawari-8/AHI bands #13 (10.4 μm) (left), #14 (11.2 μm) (middle) and #15 (12.4 μm) (right).

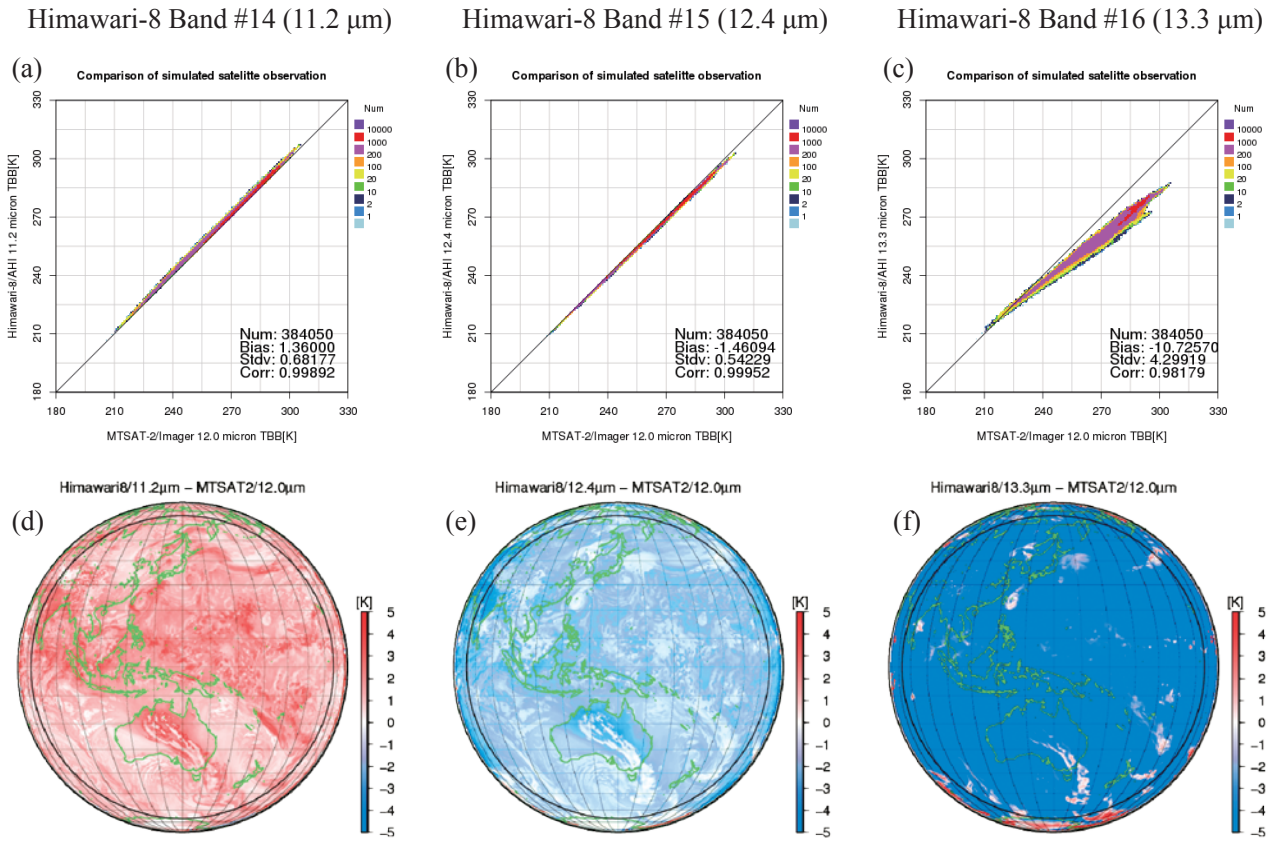

Fig.9: Same as Fig.4, except for comparisons of the simulated brightness temperatures for MTSAT-2/Imager IR2 (12.0 μm) against those for Himawari-8/AHI bands #14 (11.2 μm) (left), #15 (12.4 μm) (middle) and #16 (13.3 μm) (right).

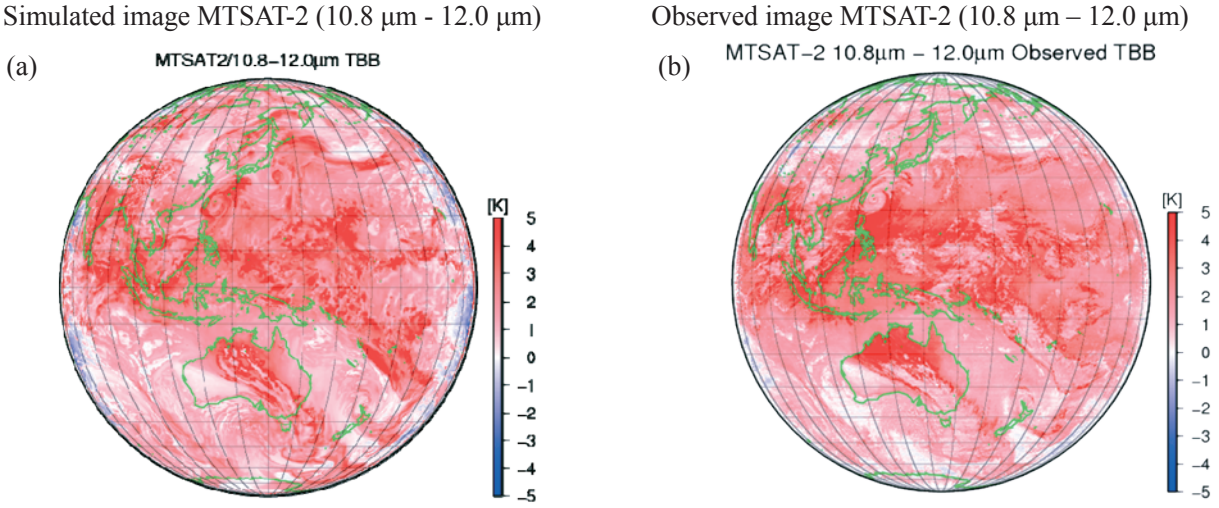

Fig.10: Comparison of brightness temperature differences for MTSAT-2/Imager SW bands from (a) the simulation and (b) observation.

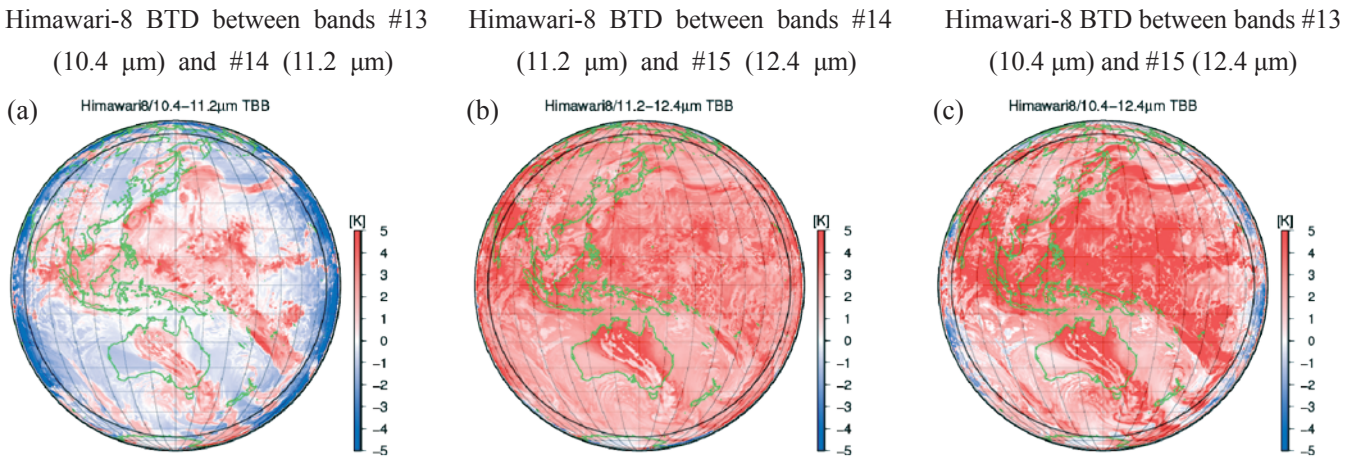

Fig.11: A comparison of simulated BTD images for Himawari-8/AHI SWs. The images are for: (a) bands #13-#14, (b) bands #14-#15 and (c) bands #13-#15.

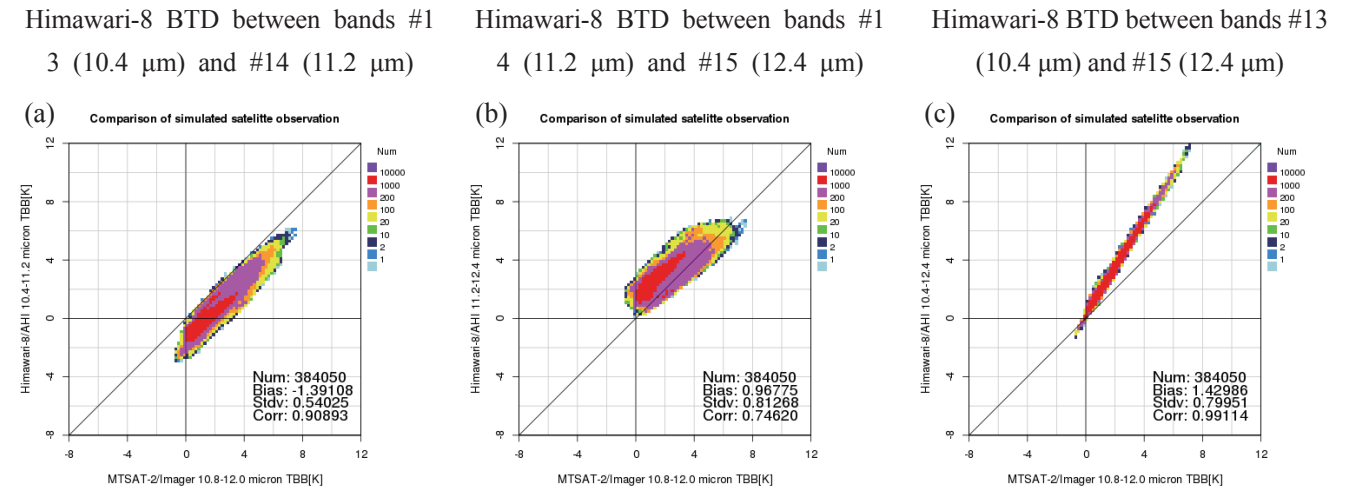

Fig.12: 2-dimensional histograms with MTSAT-2/Imager SW simulated BTD on the horizontal axis, and Himawari-8/AHI simulated BTD between (a) bands #13-#14, (b) bands #14-#15 and (c) bands #13-#15 on the vertical axis

4. Summary

In this study, Himawari-8 bands compatible with those of MTSAT-2 (i.e., having similar characteristics) were selected for the benefit of users who will continue to use only the same bands as those provided by MTSAT-2, and for HimawariCast, which disseminates a limited number of bands.

Simulated images derived by radiative transfer model RSTAR using GSM numerical weather prediction data were utilized to compare the Himawari-8 bands with those of MTSAT-2. In visual comparison with actual observed images, the simulated images of MTSAT-2 were found to be generally realistic.

A snapshot of the simulated image, which included a variety of weather and solar illumination conditions, was used for the comparison. The selection of compatible bands focused on there being a high correlation between the simulated image for the two instruments, and aspects

regarding band usage were also taken into account.

For the VIS band (0.68 μm) of MTSAT-2, band #3 (0.64 μm) of Himawari-8 was selected as the compatible band. The comparisons shown in the 2-dimensional histogram and full-disk map indicate good agreement with band #3, whose central wavelength and SRF are close to that of the VIS band.

For IR4 band (3.7 μm), band #7 (3.9 μm) was selected, this being the only candidate. Due to the effects of solar refletion, the difference is larger in daytime, especially over clouds. During nighttime, the difference is comparatively small.

For the IR3 (WV) band (6.8 μm), band #8 (6.2 μm) was selected. Visual comparisons focusing on water vapor shade patterns, which reflect the stucture of the upper troposhere, show bands #8 (6.2 μm) and #9 (6.9 μm) to be candidates. From the comparisons shown in the 2-dimensional histograms, band #8, with the highest correlation to IR3, was adopted as the best band. Note that band #8 brightness temperature is slightly colder than for IR3 because the layer of peak sensitivity is higher than IR3.

Both the IR1 (10.8 μm) and IR2 (12.0 μm) bands were compared with the Himawari-8 "atmospheric window" bands, and the combination of bands to be used as a split window (SW) were also considered. IR1 has a high correlation to bands #13 (10.4 μm) and #14 (11.2 μm), and IR2 a high correlation to bands #14 and #15 (12.4 μm). The brightness temperature difference (BTD) for IR1 and IR2 was compared with each combination of two of the three bands #13, #14 and #15 as the SW. The band #13 and #15 combination shows the highest correlation to that of IR1 and IR2. The BTD image for this combination shows higher contrast than that for MTSAT-2 SW, and this is beneficial to the detection of cirrus and volcanic ash, etc. Taking the above results into account, band #13 was selected as the compatible band for IR1 and band #15 was selected for IR2. Although band #13 is slightly colder than IR1, this difference is less noisy in spatial terms.

The selected VIS and IR compatible bands are summarized in Table 4. These bands can be used in the same manner as the corresponding MTSAT-2 band with similar characteristics. Nevertheless, it should be noted that these bands are not exactly identical to the MTSAT-2 bands.

Table 4: VIS and IR bands of Himawari-8/AHI compatible with those of MTSAT-2/Imager

MTSAT-2/Imager		Himawari-8/AHI	
VIS	0.68 μm	Band #3	0.64 μm
IR1	10.8 μm	Band #13	10.4 μm
IR2	12.0 μm	Band #15	12.4 μm
IR3	6.8 μm	Band #8	6.2 μm
IR4	3.7 μm	Band #7	3.9 μm

Acknowledgement

The authors would like to express their appreciation to Professor NAKAJIMA, Teruyuki and Dr. TAKENAKA, Hideaki of the Tokyo University, Atmosphere and Ocean Research Institute (AORI), who provided helpful comments and suggestions regarding development of the satellite observation simulator using RSTAR.

The authors are grateful to OpenCLASTR project for enabling RSTAR (system for transfer of atmospheric radiation) package to be used in this study.

References

Bormann, N., A. H.-Carrascal, R. Borde, H.-J. Lutz, J. A. Otkin, and S. Wanzong, 2014: Atmospheric Motion Vectors from Model Simulations. Part I: Methods and Characterization as Single-Level Estimates of Wind. J. Appl. Meteor. Climatol., 53, 47-64.

Clark, R.N., Swayze, G.A., Wise, R., Livo, E., Hoef en, T., Kokaly, R., Sutley, S.J., 2007: USGS dig ital spectral library splib06a: U.S. Geological Su rvey, Digital Data Series 231, Available at http:/ /speclab.cr.usgs.gov/spectral.lib06/ds231.

JMA, 2003: JMA HRIT Mission Specific Implementa tion (Issue 1.2, 1 January, 2003). Available at h ttp://www.data.jma.go.jp/mscweb/en/operation/type/ HRIT/JMA_HRIT_Issue1.2.pdf.

JMA, 2010: JMA LRIT Mission Specific Implementation (Issue 7, 1 July, 2010). Available at http://www.data.jma.go.jp/mscweb/en/operation/type/LRIT/JMA_LRIT_Issue7.pdf.

JMA, 2013: Outline of the operational numerical weather prediction at the Japan Meteorological Agency. Appendix to WMO Numerical Weather Prediction Progress Report. Japan Meteorological Agency, Tokyo, Japan. Available at http://www.jma.go.jp/jma/jma-eng/jma-center/nwp/outline2013-nwp/index.htm.

JMA, 2014: Himawari-8/9 data distribution/dissemination plan (13 May 2014). Available at http://www.jma.go.jp/jma/jma-eng/satellite/news/himawari89/himawari89_distribution_plan.html.

Lindsey, D. T., T. J. Schmit, W. M. MacKenzie, Jr., C. P. Jewett, M. M. Gunshor, L. Grasso, 2012: 10.35 μm: atmospheric window on the GOES-R Advanced Baseline Imager with less moisture attenuation, Journal of Applied Remote Sensing, 6:1, 12.

Maki, T., A. Ebita, T. Ishimizu, K. Nagata, M. Ikegami and T. Sasaki, 2008: The Daily 3D Ozone produced by the Chemical Transport Model for JRA-25. Extended abstracts of Workshop on the Third WCRP Reanalysis Conference, Tokyo, Japan, 28 January - 1 February, 2008.

Miyamoto, K., M. Nakagawa, T. Nakamura, Y. Kitagawa, T. Komori, 2009: Physical process, Convection. Numerical Prediction Division Report. Supplement 55, 68-82. (in Japanese)

Nakajima, T. and M. Tanaka, 1986: Matrix formulation for the transfer of solar radiation in a plane-parallel scattering atmosphere. J. Quant. Spectrosc. Radiat. Transfer, 35, 13-21.

Nakajima, T., and M. Tanaka, 1988: Algorithms for radiative intensity calculations in moderately thick atmospheres using a truncation approximation, J. Quant. Spectrosc. Radiat. Transfer, 40, 51-69.

Otkin, J. A., D. J. Posselt, E. R. Olson, H.-L. Huang, J. E. Davies, J. Li, and C. S. Velden, 2007: Mesoscale Numerical Weather Prediction Models Used in Support of Infrared Hyperspectral Measurement Simulation and Product Algorithm Development. J. Atmos. Oceanic Technol., 24, 585-601.

Owada, H., 2006: Simulated satellite image. Meteorological Research Note, 212, 105-120. (in Japanese)

Schmit, T. J., M. M. Gunshor, W. P. Menzel, J. Li, S. Bachmeier, and J. J. Gurka, 2005: Introducing the next-generation Advanced Baseline Imager on GOES-R. Bull. Amer. Meteor. Soc., 86, 1079-1096.

Stamnes, K., S.-C. Tsay, W. Wiscombe, and K. Jayaweera, 1988: Numerically stable algorithm for discrete-ordinate-method radiative transfer in multiple scattering and emitting layered media, Appl. Opt., 27, 2502-2509.

Tahara, Y., 2008: Central Wavelengths and Wavenumbers and Sensor Planck Functions of the GMS and MTSAT Infrared Channels, Meteorological Satellite Center technical note, 50, 51-59. (in Japanese)

Vermote, E. F., S. Y. Kotchenova and J. P. Ray, 2011: MODIS Surface Reflectance User's Guide, Available at http://modis-sr.ltdri.org/products/MOD09_UserGuide_v1_3.pdf.

Yang, P., K. N. Liou, K. Wyser and D. Mitchell, 2000: Parameterization of the scattering and absorption properties of individual ice crystals. J. Geophys. Res., 105, D4, 4699-4718.

Yokota, H., M. Sasaki, 2013: Introduction to Himawari-8 and 9, Meteorological Satellite Center technical note, 58, 121-138. (in Japanese)

ひまわり 7 号の可視・赤外バンドに対応する ひまわり 8 号のバンド検討

村田 英彦* 、髙橋 昌也* 、髙坂 裕貴**

要旨

気象庁は、ひまわり 8 号および 9 号を、2014 年および 2016 年に打ち上げ、ひまわり 8 号の運用を 2015 年に開始する計画である。ひまわり 8 号および 9 号に搭載される可視赤外放射計（Advanced Himawari Imager; AHI）は、MTSAT-2（ひまわり 7 号）と比較して大幅に観測機能が強化され、バンド数は、ひまわり 7 号の 5 バンドに対し、16 バンドに増加する。ひまわり 8 号の運用開始後も、ひまわり 7 号と同じバンドのみを引き続き使用するユーザーのため、またひまわりキャストで限られた数のバンドを配信するため、ひまわり 7 号の各バンドが、ひまわり 8 号のどのバンドに対応しているかについて検討を行った。検討では、放射伝達モデルを用い、数値予報データ等を入力データとして、ひまわり 7 号および 8 号の疑似観測データを作成し、両者の比較を行うことで、対応バンドを決定した。

* 気象衛星センターデータ処理部システム管理課

** 気象庁予報部数値予報課